Hypersonic Boundary Layer Transition Measurements Using $NO_2 \rightarrow NO$ Photo-dissociation Tagging Velocimetry

Brett F. Bathel[1], Craig T. Johansen[2], Paul M. Danehy[3], Jennifer A. Inman[4], Stephen B. Jones[5]
NASA Langley Research Center, Hampton, Virginia, 23681-21991

and
Christopher P. Goyne[6]
University of Virginia, Charlottesville, Virginia, 22904

Measurements of instantaneous and mean streamwise velocity profiles in a hypersonic laminar boundary layer as well as a boundary layer undergoing laminar-to-turbulent transition were obtained over a 10-degree half-angle wedge model. A molecular tagging velocimetry technique consisting of a $NO_2 \rightarrow NO$ photo-dissociation reaction and two subsequent excitations of NO was used. The measurement of the transitional boundary layer velocity profiles was made downstream of a 1-mm tall, 4-mm diameter cylindrical trip along several lines lying within a streamwise measurement plane normal to the model surface and offset 6-mm from the model centerline. For laminar and transitional boundary layer measurements, the magnitudes of streamwise velocity fluctuations are compared. In the transitional boundary layer the fluctuations were, in general, 2-4 times larger than those in the laminar boundary layer. Of particular interest were fluctuations corresponding to a height of approximately 50% of the laminar boundary layer thickness having a magnitude of nearly 30% of the mean measured velocity. For comparison, the measured fluctuations in the laminar boundary layer were approximately 5% of the mean measured velocity at the same location. For the highest 10% signal-to-noise ratio data, average single-shot uncertainties using a 1 µs and 50 µs interframe delay were ~115 m/s and ~3 m/s, respectively. By averaging single-shot measurements of the transitional boundary layer, uncertainties in mean velocity as low as 39 m/s were obtained in the wind tunnel. The wall-normal and streamwise spatial resolutions were 0.14-mm (2 pixel) and 0.82-mm (~11 pixels), respectively. These measurements were performed in the 31-inch Mach 10 Air Wind Tunnel at the NASA Langley Research Center.

I. Introduction

DEVELOPMENT of physics-based computational fluid dynamic (CFD) tools having the capability to predict the onset of laminar-to-turbulent transition in a hypersonic boundary layer must ultimately be validated against experimental data that resolves the dynamic (velocity) and thermodynamic (pressure, temperature, and species fraction) states of the flow as functions of time and space. For CFD validation against velocity measurements, it is desirable that the measurement technique used to obtain velocity information be able to function in the extreme conditions present in a hypersonic flowfield without: 1) perturbing the flow itself and 2) failing due to the relatively large mechanical and thermal loads placed upon the measurement device. Some recent roughness-induced boundary layer transition experiments [1,2] have successfully used both hot-wire and Pitot probes to characterize the transition process in Mach 3.5 and 6 facilities, respectively. However, in higher Mach number test facilities, the use of such physical probes can suffer from the described deficiencies. For validation against direct thermodynamic property measurement, it is desirable that the measurement technique be able to quantify the pressure, temperature, species fraction and/or density without inducing a change in the chemical composition of the gas mixture, in addition to the

[1] Graduate Student, NASA Graduate Co-op, National Institute of Aerospace, and University of Virginia, Hampton, Virginia, AIAA Student Member.
[2] Post-Doctoral Researcher, National Institute of Aerospace and NSERC, AIAA Member.
[3] Research Scientist, Advanced Sensing and Optical Measurement Branch, MS 493, AIAA Associate Fellow.
[4] Research Scientist, Advanced Sensing and Optical Measurement Branch, MS 493, AIAA Member.
[5] Research Technician, Advanced Sensing and Optical Measurement Branch, MS 493.
[6] Research Associate Professor, Mechanical and Aerospace Engineering, Aerospace Research Laboratory, PO Box 400248, AIAA Associate Fellow.

items mentioned previously. The measurement technique must also have a time response that is sufficiently short to quantify transient flow properties (i.e. fluctuations in velocity, temperature, etc.), have a sufficient spatial resolution such that variations in dynamic and thermodynamic properties in the region of interest can be resolved, and be able to resolve such properties away from the surface. Finally, it is desired to make many such measurements simultaneously along a line, a plane or in a volume. Based upon these criteria, laser-based optical measurement techniques become an attractive alternative to traditional physical probe-based measurements.

While laser-based optical measurement techniques have the potential to provide quantitative, off-body flowfield information, care must be taken to select a technique appropriate for the flow conditions of interest in order to ensure adequate signal-to-noise levels. For velocity measurements in a hypersonic boundary layer flow undergoing laminar-to-turbulent transition, molecular tagging velocimetry (MTV) is a particularly attractive technique, as it allows for instantaneous measurement of 1 or 2 components of velocity at multiple locations simultaneously within the flow. The measurement is made by determining the displacement of spatial patterns between two images separated by some time delay. The images can be formed by a series of one or more lines in the flow. The lines themselves are created either by optically promoting some form of molecular excitation [3-9] or optically suppressing [10,11] signal. Several variants of the MTV technique exist (see Ref. [12] for a more detailed listing of MTV methods), each of which depend on how the molecules are tagged and what spatial pattern is written to the flow.

One MTV method in particular, which uses fluorescence tagging of nitric oxide (NO), has recently been applied [13,14] at the NASA Langley Research Center's 31-Inch Mach 10 Air Wind Tunnel. In these experiments, measurements of both average and instantaneous velocity profiles were made in a hypersonic laminar boundary layer on a 10° half-angle wedge. For the conditions of these experiments, the lifetime of the signal generated was long enough to allow measurable signal in both initial and 500 ns delayed frames, requiring only a single laser source for molecular tagging with uncertainty levels less than 100 m/s and 30 m/s for single-shot and mean measurements, respectively. However, for the same wind tunnel facility and model, obtaining measurements in a hypersonic boundary layer undergoing laminar-to-turbulent transition requires a flow that is at higher Reynolds numbers. To achieve higher Reynolds numbers in the 31-Inch Mach 10 facility, either the facility stagnation pressure, model angle-of-attack (AoA), or both must be increased. Either change results in higher post-shock static pressures. For the conditions of this experiment, increasing the post-shock static pressure proportionally reduced the fluorescence lifetime. The conditions at which laminar-to-turbulent transition will occur will cause a reduction in lifetime of 75% or more when compared to lifetimes of the previous experiments [13,14]. Therefore, to measure velocity profiles within this transitioning hypersonic boundary layer, an alternative to the single laser, single excitation step measurement must be found.

The purpose of this paper is to detail the application of the $NO_2 \rightarrow NO$ photo-dissociation molecular tagging velocimetry technique in NASA Langley's 31-Inch Mach 10 Air Tunnel to measure instantaneous velocity profiles in a hypersonic boundary layer undergoing laminar-to-turbulent transition. This technique has been both developed and demonstrated by several researchers [15-19] and consists of a write step in which a spatial pattern is written onto the gas flowfield. This step is followed by two read steps which induce fluorescence within the spatial pattern. To our knowledge, this paper represents the first application of the technique in a transitioning hypersonic boundary layer.

II. Experimental Setup

A. Wind Tunnel Facility

The 31-Inch Mach 10 Air Tunnel is an electrically-heated blowdown facility located at NASA Langley Research Center in Hampton, Virginia, USA. The full details of this facility can be found in the paper by Micol [20], a brief summary of which is provided here. The facility has a nominal Mach number of 10 and a 31-inch square test section and operates on electrically heated, compressed air. Large windows, transparent in the ultraviolet, form three walls (including top, side and bottom) of the test section with the fourth wall formed by the model injection system. The top window allows for the laser sheet to pass through the tunnel test section, while the side window allows for imaging of the flow region of interest. The model is attached at the rear to a sting, which is subsequently side-mounted to the fourth wall. Run durations for the experiments were about one minute. A single nominal facility stagnation pressure, P_0, of 4.96 MPa (720 psia) was investigated. The nominal stagnation temperature, T_0, was 1,000 K (1,800 Rankine). Based upon the stagnation conditions, the approximate freestream Mach number was 9.81, the approximate freestream velocity was 1400 m/s, the approximate freestream unit Reynolds number (Re_∞) was 3.4×10^6 m^{-1}, the approximate freestream static pressure was 130 Pa (18.9×10^{-3} psi), and the approximate freestream temperature was 51 K (92 °R) [20].

B. PLIF Imaging System

In this experiment, two different Nd:YAG pumped dye lasers were used. The first was a 10-Hz pulsed Spectra Physics Pro-250 Nd:YAG laser that was used to pump a Sirah Cobra Stretch dye laser at 532 nm to achieve a 622 nm output beam. This output was mixed with a portion of the 355-nm light produced by the Nd:YAG in a Sirah Frequency Conversion Unit to produce about 5 mJ/pulse of a 226-nm beam, of which about 0.5 mJ/pulse was used in a laser sheet. This beam is referred to herein as the 1st probe beam. It had a spectral line width of approximately 0.07 cm^{-1}. The remaining portion (approximately 11-14 mJ/pulse) of the 355 nm beam, referred to hereafter as the pump beam, was diverted by a pick-off window to the wind tunnel test section. A second pulsed laser system consisting of the same hardware, but using a Spectra Physics Pro-230 Nd:YAG laser, was used to generate a variable-delayed secondary 226 nm beam, referred to hereafter as the 2nd probe beam, with a similar energy as the first. The duration of each probe beam pulse at this wavelength was approximately 9.5 ns.

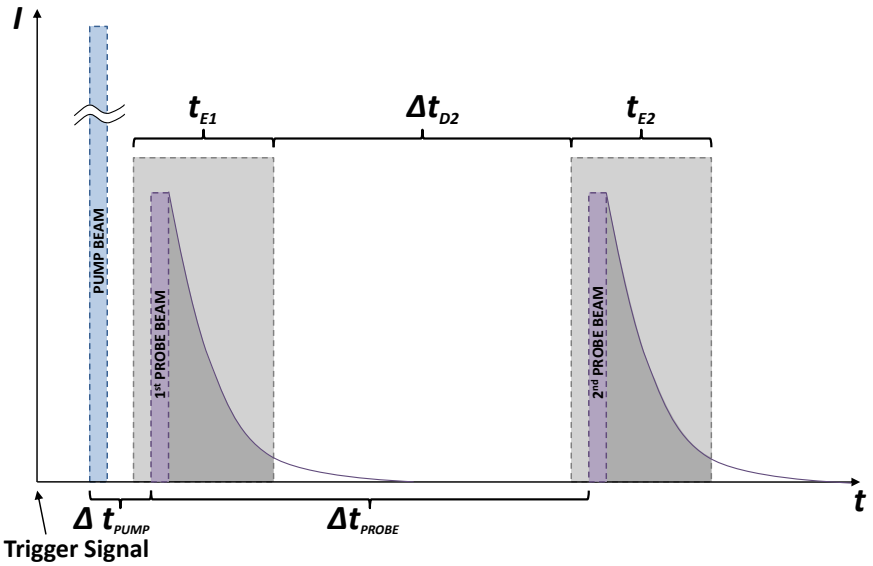

Fig. 1. Timing schematic for pump beam, both probe beams, 1st and 2nd exposures, inter-frame delay. The vertical axis represents relative intensity. The 355 nm pump beam does not generate a signal, but is show in the diagram to describe the timing of the pulses.

Both the 1st and 2nd probe beams were aligned to be collinear and followed a delay path that was then aligned adjacent to and parallel to the pump beam at the test section. The delay path was such that the time interval, Δt_{PUMP}, between the arrival of the pump beam and arrival of the subsequent 1st probe beam was approximately 38 ns. The delay between the 1st probe beam and subsequent 2nd probe beam, Δt_{PROBE}, was 1 μs in the wind tunnel experiments and was varied in the static gas experiments. Figure 1 presents a timing schematic showing the relative positions and intensities of the pump and probe beams used in this experiment.

In order to generate multiple lines of NO via photo-dissociation of NO_2, the pump beam was first passed through a 300-mm cylindrical lens then collimated by a 1-m spherical lens placed about 1 meter from the test article. The collimated 355-nm light from the pump beam was then passed through a portion of a 50-mm-long, LaserOptik diffusion-welded lens array consisting of 25, 1-m focal length cylindrical lenses. Each lens element of the array was approximately 2-mm wide and had an anti-reflection coating. To ensure the photo-dissociation of NO_2 (and subsequent generation of NO) along multiple spatial lines, the expansion of the 355 nm pump beam in one direction through the cylindrical lens and subsequent collimation with spherical lens was such that it filled the 15 lens elements in the center of the lens array. The spherical lens also served to focus the other axis of the beam. The lens array then focused the light into 15 lines aligned in the streamwise direction and having a nominal 15° angle of incidence with respect to the model surface. The lines generated by the pump beam typically had widths of approximately 0.7-mm at FWHM (full width at half maximum) and thickness of 0.7-mm. The lines were slightly diverging, resulting in a separation distance between the lines of approximately 2.3-mm.

To electronically excite the NO generated by the pump beam, the probe beams were passed through a 150-mm cylindrical lens and collimated with the same 1-m spherical lens used to collimate the 355 nm light from the pump beam. The 226 nm laser sheets were offset a few mm from the 355 nm laser sheet so that the 226 nm laser sheets did not pass through the lens array. The separation between the 150-mm cylindrical lens and the 1-m spherical lens was such that the width of the sheet was approximately 7.6-cm and the thickness was approximately 0.5-mm in the interrogation region. Furthermore, the 355 nm sheet was rotated very slightly (a few degrees) with respect to the 226 nm sheets to ensure that the beams would be in alignment even if vibrations caused the sheets to move relative to each other during the run. The electronic transition selected for this measurement corresponded to the A←X(0,0)

band of NO near 226.25 nm. Specifically, the overlapping $Q_{11}(1.5)$ and $P_{21}(1.5)$ absorption lines were selected for excitation.

To image the probed lines, a 12-bit Cooke DiCam-PRO camera, with an intensified 1280x1024 pixel array interline progressive scan CCD, was used. For this experiment, only a portion of the full CCD was used for acquiring the images in order to increase the framing rate. An F/2.0 100 mm focal length lens from Bernhard Halle Nachfolger GmbH was used. The camera was operated in double shutter mode and acquired an image pair having a 900 ns interframe delay, Δt_{D2}, between the end of the 1st exposure and beginning of the 2nd exposure, with each exposure (t_{E1} and t_{E2}, respectively) being 100 ns in duration. Each exposure was timed to overlap the 1st and 2nd probe beams. The duration of each exposure and the delay between them resulted in an effective time separation between each image of 1 μs. The signal collected during each exposure is represented by the area under the initial probe beam excitation (dashed rectangular grey box) and exponential signal intensity decay curve in Fig. 1.

C. Wind Tunnel Model

The flow experiment was conducted using a 10° half-angle wedge model with a sharp leading edge, similar to that described in Refs. [14,21]. Table 1 provides a description of the test conditions. For the tripped experiment, a 1-mm tall, 4-mm wide cylindrical boundary layer trip was positioned along the centerline 75.4-mm downstream of the leading edge (measured to the center axis-of-symmetry of the trip) to deflect and perturb the boundary layer gas. The ratio of trip height, k, to boundary layer thickness, δ, for this experiment was approximately 1.05. The trip location was the same as that found in Refs. [14,21]. The 100% NO_2 gas was seeded into the boundary layer from an 11-mm-long, 0.81-mm-wide spanwise slot located 29.4-mm downstream of the leading edge. A 50.8-mm outer diameter, 6.4-mm thick quartz window centered 114.3-mm downstream of the leading edge and about the spanwise axis of symmetry was mounted flush to the model surface. The window had a 2.8 mm chamfer, resulting in a 46.8-mm inner diameter portion of the window to be exposed at the surface. Figure 2 shows an image of the model with the mounted window. The use of the UV-transparent window prevented damage to the model's otherwise black painted surface and reduce the laser scatter generated by the focused 355 nm pump beam.

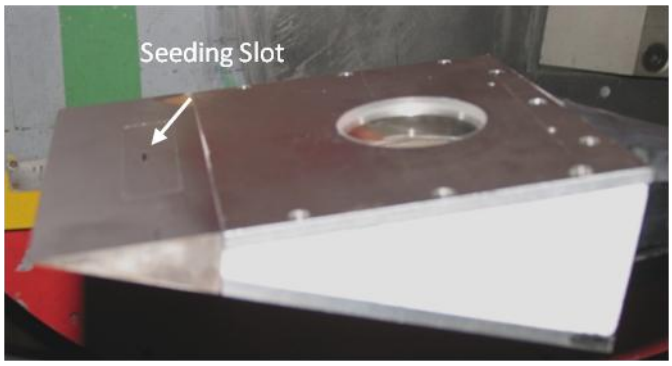

Fig. 2. Wedge model with 50.8-mm diameter, 6.4-mm thick window mounted to upper surface. No trip is mounted to the model.

Table 1. Test parameters.

Test – Run	Trip	k	k/δ	M_e	Re_∞	Flow Rate (Composition)	Test Type
443 – 25	-	-	-	4.2	$3.4x10^6$ m^{-1}	300 SCCM (100% NO)	Flow Visualization
477 – 33	-	-	-	4.2	$3.4x10^6$ m^{-1}	760 SCCM (100% NO_2)	$NO_2 \xrightarrow{h\nu_{355\,nm}} NO_{v=0}$
443 – 19	Cylinder	1-mm	1.05	4.2	$3.4x10^6$ m^{-1}	300 SCCM (100% NO)	Flow Visualization
477 – 35	Cylinder	1-mm	1.05	4.2	$3.4x10^6$ m^{-1}	228 SCCM (100% NO_2)	$NO_2 \xrightarrow{h\nu_{355\,nm}} NO_{v=0}$

III. Image Processing and Analysis

A. Initial Image Processing

The image magnification and spatial resolution were measured by acquiring an image consisting of a matrix of square marks separated at 0.25-inch spatial intervals, known as a *dotcard* and described in Ref. [22]. The magnification for Runs 33 and 35 of Test 477 was 14.0±0.04 pixels/mm. Additional data sets acquired with varying time delays, Δt_{PROBE}, and static pressures were also obtained for the purpose of estimating the uncertainty in determining the spatial shift of the tagged lines between two exposures. Hereafter, this is referred to as the spatial velocity uncertainty and is a function of the signal-to-noise ratio. These data sets corresponded to Runs 7 – 16 of Test 477, which had a magnification of approximately 15.1±0.07 pixels/mm.

To correct for optical and perspective distortion of the images, the image of the dotcard in the test section was acquired with the camera and compared to a corresponding undistorted digital image of the same dotcard. An image

registration algorithm, UnwarpJ [23], was then used to correct the distortion. This software is a plug-in created for the image processing software, ImageJ, a freeware image processing program available from the National Institutes of Health [24].

Prior to processing each image for velocity information, a background image was subtracted from the 1st and 2nd exposure images. The background images were created by separately averaging a series of images from the 1st and 2nd exposures while the laser was blocked. Due to the shortness of the interframe delay, Δt_{D2}, used between the end of the 1st exposure and the beginning of the 2nd exposure images and the relatively long decay time of the P46 phosphor in the intensifier, some ghosting remained from the 1st exposure in the delayed image. The ghosting level was experimentally estimated to be approximately 1.2% of the signal in the 1st image. This fraction of the 1st exposure image was also subtracted from the 2nd exposure image in addition to the normal background image. A bleaching effect was observed to occur when the signal counts in the 1st exposure approached the maximum dynamic range of the camera, resulting in absences of signal in the 2nd exposure. To avoid biasing the measurement as a result of this bleaching effect, any data profiles having maximum counts of 3000 or higher were discarded.

In Runs 33 and 35, the surface of the wedge model moved slightly during acquisition of the experimental images. This was assumed to be an effect of thermal loading on the model body and sting. In Run 33, for instance, the plate surface temperature, measured using a thermocouple, increased approximately linearly from 308 K to 350 K over the course of the 38.4 second image acquisition period. This was accompanied by an observed plate displacement of approximately 1.0 mm (14 pixels), which was determined by tracking the path of scattered light at two points at the leading and trailing edges of the quartz window insert. Similarly in Run 35, the observed total vertical displacement of the model surface was approximately 0.3 mm (4 pixels). These displacements are attributed to thermal loading on the sting, which warped over the course of the run, slightly changing the position of the plate. In order to make an accurate measurement of the boundary layer velocity, the experimental images from Runs 33 and 35 were first shifted to the approximate location of the first image in each respective set of images. Although the small shift in plate position adversely affects the image processing algorithm, corresponding changes in the velocity field owing to AoA changes are negligible.

B. Velocity and Uncertainty Analysis

A general description of the computation of the velocity and associated uncertainty from the NO MTV images is provided in Refs. [13,14,25]. The modified timing procedure for the NO_2–seeding technique described in this paper requires a slightly modified derivation of both velocity and the corresponding velocity uncertainty.

Since the duration of both the 1st and 2nd exposures were the same and the temporal overlap of each exposure with the respective probe beam was kept constant, the velocity measurement was assumed to be unaffected by spatial profile distortions which might occur due to fluorescence signal decay during the time-integrated exposures, as was the case in Refs. [13,14,25]. Therefore, the velocity is defined as the measured mean magnification factor, M, times the displacement (in pixels), Δx, between the centroid of the spatial intensity distribution in the 1st and 2nd exposures divided by the temporal separation between the signal captured during the 1st and 2nd exposures, $\Delta t = \Delta t_{PROBE}$, and is denoted as:

$$V = M\frac{\Delta x}{\Delta t} \tag{1}$$

The method adopted to analyze uncertainty in velocity due to spatial uncertainties, $u_{V,\Delta x}$, in this paper is similar to that found in Ref. [25]. For a sample of instantaneous measurements, the spatial uncertainty term $u_{\Delta x}$ is composed of uncertainties in determining Δx due to: 1) flow unsteadiness resulting in measured fluctuations in Δx and 2) reduced signal-to-noise levels resulting in errors in determining the precise value of Δx due to poorly conditioned cross-correlation results. Using Equation (1), this term is:

$$u_{V,\Delta x} = \frac{\partial V}{\partial(\Delta x)} \cdot u_{\Delta x} = M\frac{1}{\Delta t} \cdot \left(t_{N-1,95\%} \cdot \sigma_{\Delta x}\right) \tag{2}$$

where $t_{N-1,95\%}$, is the student t-statistic at 95% confidence, N is the number of data points used to compute velocity at a particular point in the images, and $\sigma_{\Delta x}$ is the measured standard deviation of Δx.

In order to fully quantify the timing uncertainty, $u_{\Delta t}$, we must first determine the temporal separation between the 1st and 2nd exposures and then identify how various systematic timing errors affect the precision of the temporal separation. For both exposures, the time between initial intensity generation by the probe laser beam pulse and the

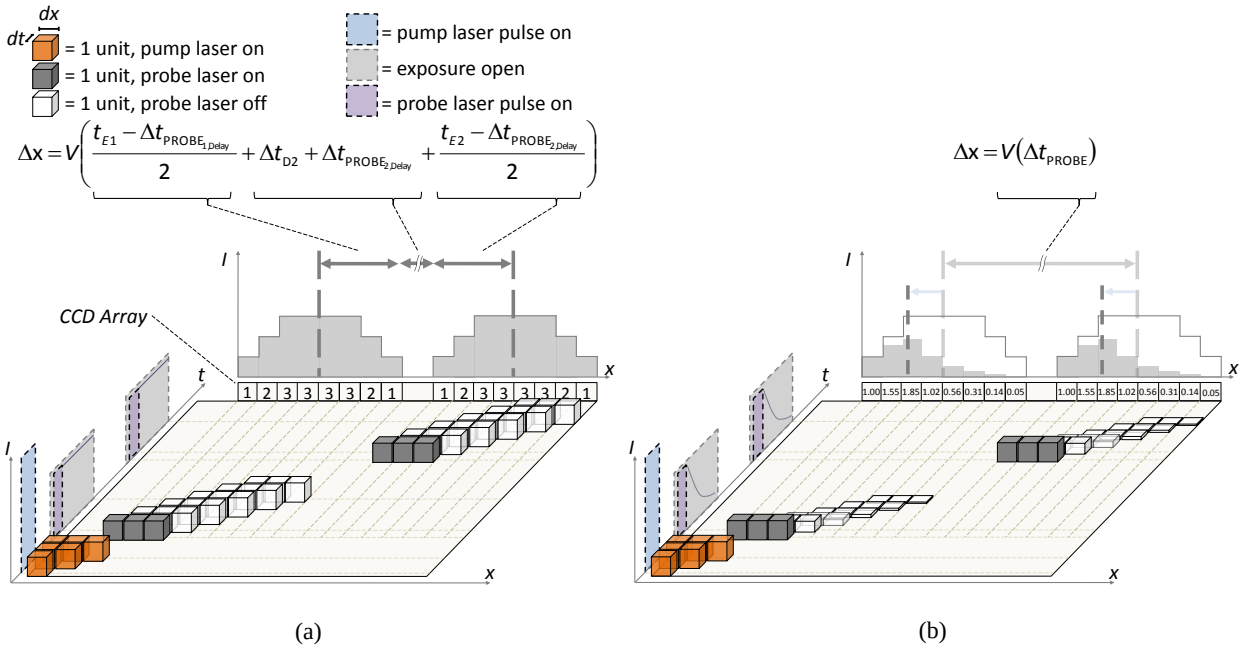

(a) (b)

Fig. 3. Idealized time-space-intensity diagram (not to scale) of generation of NO from photo-dissociation of NO_2 and subsequent excitation of NO by probe laser beams and acquisition by CCD without (a) and with (b) consideration for fluorescence decay. The decay lifetime in (b) was approximated to be 1/3 of the effective exposure duration (5/3 of *dt*).

end of the exposure is referred to as the *effective* exposure duration. During this period, the probe laser beam pulse begins to populate the excited electronic state of the NO gas during the laser pulse (t_{Pulse}). Simultaneously, photons are continually emitted from this excited state. When the probe laser beam pulse ceases, photons continue to be emitted from NO molecules transitioning from the excited to the ground electronic state. The photons emitted by the excited NO molecules along the tagged lines are collected onto the CCD from the moment the laser pulse turns on until the end of the effective exposure. The excited NO molecules can move during the exposure time, resulting in some spatial blurring. The amount of blurring is less if the gas has a lower velocity or a shorter fluorescence lifetime. If the decay of the fluorescence intensity is taken into account, the spatial intensity distributions in each exposure will also be affected, with the perceived distribution in both frames being weighted away from the direction of travel of the NO gas. Nonetheless, as will be described in detail below, if the gas velocity and fluorescence lifetime is the same in both exposures, then this blurring does not cause a systematic error in measurement. Conversely, in suddenly expanding or compressing flows, a significant error in computed velocity can occur because the velocity is not constant during the measurement interval.

Figure 3 provides an idealized representation of the $NO_2 \rightarrow NO$ photo-dissociation process, subsequent probe laser excitations, and CCD exposures. In Fig. 3a, we have assumed that the fluorescence intensity following excitation in both the 1st and 2nd exposures does not diminish over the duration of each respective exposure. Near the time origin of the intensity-time (*I*-*t*) axis, the pump beam is turned on for 2 time units, generating a train of NO molecules from the NO_2 gas, which are represented by the orange blocks on the time-space (*x*-*t*) plane and moving from left to right with a velocity, *V*. The orange blocks are created at time steps t = 0, 1, and 2. When the pump beam is turned off, a train of NO that is 3 units in width has been generated via photo-dissociation of the NO_2. After approximately 1.5 time units, the 1st exposure is turned on and 0.5 time units after that, the 1st probe beam is turned on and excites the 3-unit-wide NO gas train, which is represented by the dark gray blocks on the time-space (*t*-*x*) plane. This 1st probe beam excitation period lasts for 1 time unit then turns off, with the photons generated by this excitation being simultaneously collected onto the CCD array. After the 1st probe beam is turned off, the excited molecules, now represented by the white blocks on the time-space (*t*-*x*) plane, continue to emit photons at a constant intensity as they convect. Signal from these molecules is simultaneously collected onto the CCD array until the end of the 1st exposure, occurring 5 time units after the 1st probe beam turned on. The left-most gray shaded area on the intensity-space (*I*-*x*) plane is the tagged intensity profile from the 1st effective exposure. The intensity at each spatial location on this profile represents the time integration of the fluorescence. At the first spatial location, for example, only 1 intensity unit is registered onto the CCD. This intensity unit originated from the left-most gray block that was

created during the activation of the first probe beam. At the second spatial location of the tagged intensity profile, 2 intensity units are registered onto the CCD. The first intensity unit originated from the middle gray block that was created during the activation of the first probe beam. The second intensity unit, however, was produced from the fluorescent molecules that were originally created on the left-most gray block during the activation of the probe beam, but was then convected 1 spatial unit to the right at the subsequent time unit. This integration at each spatial location is applied for the duration of the exposure and the final tagged intensity profile takes the approximate form of a symmetric trapezoid with its center indicated by the dashed gray vertical line. After the end of the 1st exposure, a period of time corresponding to the interframe delay (Δt_{D2}) passes, which is then followed by a 2nd exposure, probe beam excitation, and CCD signal acquisition sequence having the same timing and relative spatial intensity distribution (although shifted due to the convective velocity) as the 1st sequence. The total displacement measured between the two spatial intensity profiles captured in the 1st and 2nd exposures is given by the equation in Fig. 3a.

If the effect of fluorescence decay is included in the idealization, as shown in Fig. 3b, the measured displacement, Δx, occurring between the 1st and 2nd exposures remains the same. Note that the sequence shown in the (I-t) plane in Fig. 3b is similar to the schematic shown in Fig. 1. However, the perceived signal intensity distribution in each exposure in the (I-x) plane appears to be shifted away from the direction of travel of the NO gas molecules as is shown in Fig. 3b. If the fluorescence lifetime is small relative to the duration of each exposure and if the temporal position of the probe beams are well within the bounds of each exposure (as in Fig. 3b), then it is more convenient to characterize the total displacement measured between the two spatial intensity profiles using the simple equation in Fig. 3b.

As shown in Fig. 1 and Fig. 3, the effective exposure durations, $(t_{E1} - \Delta t_{PROBE_{1,Delay}})$ and $(t_{E2} - \Delta t_{PROBE_{2,Delay}})$, are defined to be the difference between the actual exposure duration and the delay occurring between the moment the exposure turns on and the moment the respective probe laser beam pulse excitation begins. Prior to this period, which will be referred to herein as the i^{th} probe beam delay, no signal is collected by the CCD. Due to this i^{th} probe beam delay, the *effective* interframe delay between the collection of signal by the CCD in the 1st and 2nd exposures is the sum of the interframe delay, Δt_{D2}, and the 2nd probe beam delay, $\Delta t_{PROBE_{2,Delay}}$. The total temporal separation between images is also equal to the delay between the two probe laser pulses, Δt_{PROBE}. Using the definitions for effective exposures and effective interframe delay, the total time separation between exposures using the geometric relations shown in Fig. 3 is:

$$\Delta t = \frac{t_{E1} - \Delta t_{PROBE_{1,Delay}}}{2} + \left(\Delta t_{D2} + \Delta t_{PROBE_{2,Delay}}\right) + \frac{t_{E2} - \Delta t_{PROBE_{2,Delay}}}{2} = \Delta t_{PROBE} \tag{3}$$

In our experiment, we assume our experimental conditions result in a process similar to that presented in Fig. 3b, where the fluorescence lifetime is small relative to the effective exposure duration and each of the probe laser pulses reside well within the bounds of their respective exposures. In fact, the fluorescence lifetime is approximately 1/3 as long as the exposure. Based upon this assumption, the uncertainty in velocity due to the temporal uncertainties is assumed to be a function of small systematic errors caused by the laser system jitter and its triggering device (Labsmith LC-880 timing generator) only. This uncertainty is insensitive to jitter in the camera timing (both the exposure time, t_{Ei} and interframe delay, Δt_{D2}).

$$u_{\Delta t} = \sqrt{\left(u_{\Delta t_{PROBE_{1,Delay}}}\right)^2 + \left(u_{\Delta t_{PROBE_{2,Delay}}}\right)^2} \tag{4}$$

In Equation 4, the i^{th} probe beam delays ($\Delta t_{PROBE_{i,Delay}}$) are a result of systematic errors caused by the timing circuits in the laser system and triggering device (Labsmith LC-880). Therefore, the uncertainty of the i^{th} probe beam delay is a function of uncertainty in both the timing of the trigger delay from the LC-880 ($u_{\Delta t_{Trigger_i}}$) supplied to the laser and the laser pulse timing ($u_{t_{Pulse_i}}$).

$$u_{\Delta t_{PROBE_{i,Delay}}} = \sqrt{{u_{\Delta t\,Trigger_i}}^2 + {u_{t_{Pulse_i}}}^2} \tag{5}$$

Since the i^{th} probe beam trigger delay and laser pulse timing have the same value for each probe beam, the terms in Equation 4 can be combined into a single equation with the resulting time uncertainty using Equations 3 and 4 given by:

$$u_{\Delta t} = \sqrt{2 \cdot \left[{u_{\Delta t_{Trigger}}}^2 + {u_{t_{Pulse}}}^2 \right]} \tag{6}$$

Table 2 provides a listing of the individual temporal uncertainties used in Equation 6, which are based on manufacturer specifications.

Table 2. Individual temporal uncertainties.

Probe Beam Trigger Delay Jitter, $u_{\Delta t_{Trigger}}$	±0.2 ns
Probe Laser Beam Jitter, $u_{t_{Pulse}}$	±1 ns

Using the definition provided in Equation 1 and the derivation provided in Equation 6, the uncertainty in the measured velocity due to temporal uncertainty is:

$$u_{V,\Delta t} = \frac{\partial V}{\partial (\Delta t)} \cdot u_{\Delta t} = -M \frac{\Delta x}{(\Delta t)^2} \cdot u_{\Delta t} \tag{7}$$

The uncertainty due to magnification, $u_{V,M}$, was determined by making 12 measurements at various vertical positions across the dotcard image and calculating the standard deviation, σ_M, of the mean magnification, M. The magnification uncertainty is calculated as:

$$u_{V,M} = \frac{\partial V}{\partial M} \cdot u_M = -\frac{\Delta x}{\Delta t} \cdot \left(t_{11,95\%} \cdot \sigma_M \right) \tag{8}$$

To estimate the single-shot uncertainty as a function of signal-to-noise ratio, velocity images were obtained while the wind tunnel was not operating, resulting in a (nearly) static gas. For each point selected, the signal-to-noise ratio in the 1st and 2nd exposure was calculated by dividing the difference between maximum signal, ($S_{1st,2nd}$) and minimum, or "valley" ($V_{1st,2nd}$), signal counts within a 21-pixel-wide window centered about the peak value of the tagged gas line by the standard deviation ($N_{1st,2nd}$) of the signal counts within a 5x5-pixel square window centered about the location of the peak signal count. The total signal-to-noise ratio for the pair of images was then computed by taking the square-root of the product of the signal-to-noise ratios calculated for each exposure, or:

$$SNR = \sqrt{\left(\frac{S_{1st} - V_{1st}}{N_{1st}}\right)\left(\frac{S_{2nd} - V_{2nd}}{N_{2nd}}\right)} \tag{9}$$

This method of calculating the signal-to-noise ratio was chosen because it accounts for the quality of the data in both the 1st and 2nd exposures images. Figure 4 shows the measured velocity uncertainty for several probe beam time delays, Δt_{PROBE}, as a function of the signal-to-noise ratio computed using Equation 9. In this figure, the plotted velocity uncertainty was computed as the product of the standard deviation of the measured velocity, σ_V, and the student t-statistic at 95% confidence. The data presented in Fig. 4 was grouped together in signal-to-noise intervals of 0.25.

As shown in Fig. 4, as the signal-to-noise ratio increases, the measured velocity uncertainty in the tagged gas decreases linearly. This general trend is expected since the increased quality of the data in both the 1st and 2nd exposures, indicated by the signal-to-noise ratio, will result in a cross-correlation that produces a more precise estimate of displacement in the tagged line at each measurement location. Conversely, as signal-to-noise ratio decreases, the precision at which the cross-correlation can determine velocity worsens. At low signal-to-noise levels, the poor signal-to-noise ratio results in a relatively large spatial uncertainties, which is the dominant form of uncertainty. For the probe beam time delay corresponding to that used in Run 35, a linear fit to the data was generated so that an estimate of single-shot spatial velocity uncertainty could be made.

For signal-to-noise levels below ~4, the computed velocity uncertainty was observed to level off. This behavior at lower signal-to-noise levels deviates from typical uncertainty versus signal-to-noise plots (such as in Ref. [26]) in which the measured velocity uncertainty exponentially increases with decreasing signal-to-noise levels. In this work, the leveling off of velocity uncertainty at lower signal-to-noise levels was caused by a data rejection threshold that

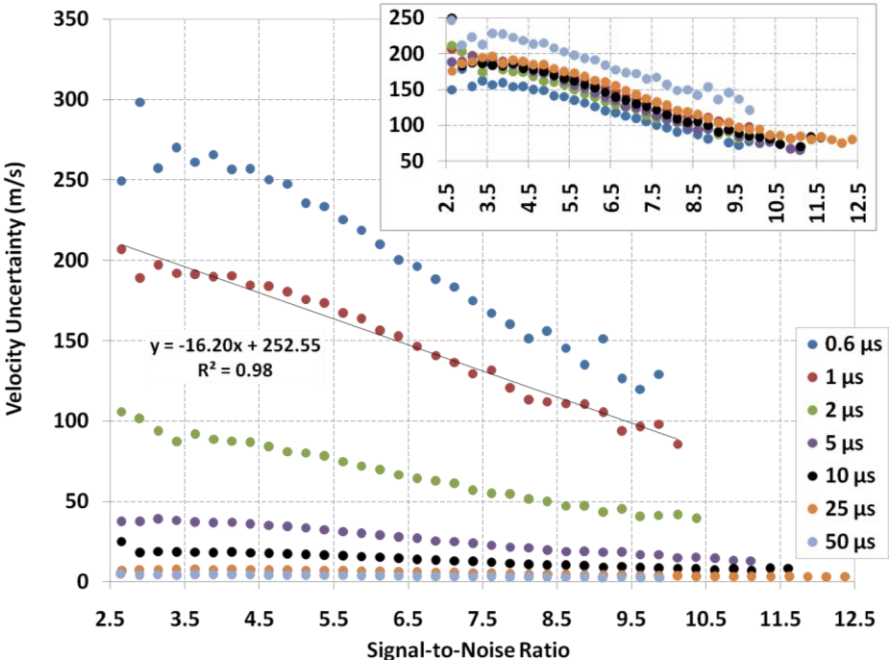

Fig. 4. Measured single-shot velocity uncertainty for several probe beam time delays as a function of signal-to-noise ratio. For the 1 µs probe beam delay data, a linear fit has been applied to estimate single-shot velocity uncertainty in Run 35. The top-right inset figure shows the velocity uncertainty as a function of signal-to-noise ratio for each probe beam time delay scaled by the delay with respect to the 1 µs delay.

estimated the quality of the cross-correlation coefficient data returned by the measurement software and was intended to limit erroneous velocity data. In fitting the data, the root-mean- square (RMS) value consisting of the R^2 value from a 2nd-order polynomial fit to the peak of the normalized cross-correlation coefficients and the peak value of the normalized cross-correlation coefficients were computed. In this analysis, any values below a threshold of 0.92 were rejected.

Figure 5 shows the data point yield, or the percent of measurement points that resulted in a valid velocity measurement, after applying the rejection threshold. At signal-to-noise ratios less than approximately 4-5, less than 10% of all the data points selected for processing will actually result in a good data point, with the balance of points being rejected due to poor quality cross-correlation velocity estimates. As the signal-to-noise ratio increases beyond approximately 5, a dramatic increase in the percentage of accepted data points is observed. As the signal-to-noise ratio surpasses a value of approximately 8, the percentage of points marked for processing actually being accepted by the software begins to level off to an approximate data yield of 80% to 90%.

When considering the effect of varying the probe beam delay, Δt_{PROBE}, on the measured uncertainty in the mean velocity shown in Fig. 4, the overall uncertainty in the velocity decreases nearly proportionally with increased Δt_{PROBE}. This result is presented in Fig. 6 (blue diamond data points), where the average uncertainty in the velocity over the signal-to-noise range of $6 \leq SNR < 8$ is plotted versus probe beam delay. If the measured velocity fluctuations had been a function of actual flow fluctuations, the measured uncertainty in velocity would be constant as Δt_{PROBE} was increased. Similarly, the mean measured velocity, denoted by the red square data points shown in Fig. 6, would level off at a constant

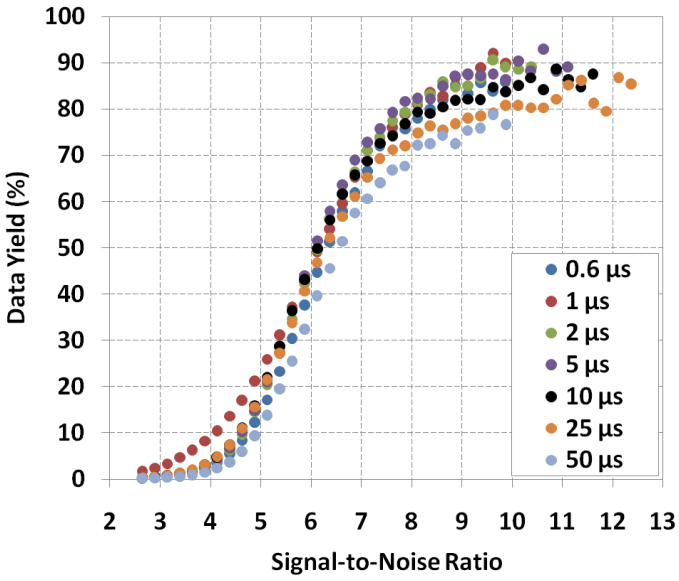

Fig. 5. Data yield resulting from software rejection threshold versus signal-to-noise ratio for several probe beam time delays.

value if there was an actual flow velocity. Thus, the fluctuations are attributed to the instrument and there is a minimum precision with which we can determine the profile displacement for a particular signal-to-noise value. Increasing Δt_{PROBE} linearly reduces our uncertainty in determining precisely the magnitude of velocity.

The accuracy of the measurement technique can be estimated from the average measured velocity, since the gas is believed to be at rest and any deviations from zero indicate an inaccuracy of the system. The analysis was performed over the signal-to-noise range of $6 \leq$ SNR < 8. This data is shown in Fig. 6 as red square data points. As Δt_{PROBE} is increased, the measured average single-shot velocity decreases proportionally with Δt_{PROBE}. It is noted in Fig. 6 that the data point corresponding to $\Delta t_{PROBE} = 1$ µs appears to be lower than the general trend suggests. This can possibly be attributed to a 33% higher gain setting used during acquisition of that particular data set. Therefore, an accuracy of 10 m/s was assumed for a 1 µs Δt_{PROBE} setting used in Runs 33 and 35, which corresponds more closely to the general trend observed in Fig. 6.

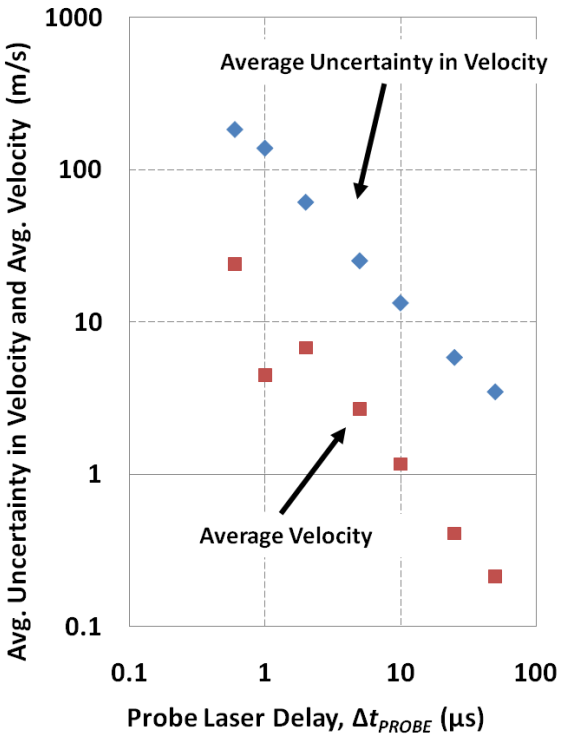

Fig. 6. Average uncertainty in velocity and average velocity as a function of Δt_{PROBE}. Averages were computed from data over the signal-to-noise range of $6 \leq$ SNR < 8 in Fig. 4.

The inset figure (top-right) in Fig. 4 shows the result of scaling each of the velocity uncertainty curves by a factor corresponding to the ratio of $\Delta t_{PROBE}/(1\ \mu s)$ for each respective data set. One µs was the delay used in Runs 33 and 35. Generally, this inset figure shows that the minimum precision with which displacement can be measured for a particular signal-to-noise value is constant, which is indicated by the nearly overlapping curves for the 1 µs, 2 µs, 5 µs, 10 µs, and 25 µs probe beam delays. The exceptions to this are the curves for the 0.6 µs and 50 µs delay times. For the 0.6 µs curve, the measured scaled velocity uncertainty is lower over the range of signal-to-noise ratio values shown. It is not currently clear as to why this particular delay time results in a lowered measured uncertainty in velocity. As for the 50 µs scaled uncertainty in velocity curve, an increased uncertainty level is observed. This increase in scaled uncertainty most likely can be attributed to gas diffusion, which becomes more influential on the measurement technique as Δt_{PROBE} is increased.

Figure 7 shows the average uncertainty in velocity, average velocity, and average signal-to-noise ratio computed using from the highest ~10% of signal-to-noise ratio values. The data was taken at 4 different static pressures while the wind tunnel was not operating. At the lowest static pressure (1.75 kPa), the signal-to-noise trend is the same as the 1 µs probe beam delay case shown in Fig. 4. When the tunnel static pressure is increased to 7.06 kPa, the uncertainty in velocity is reduced by approximately 40%, mainly because the signal-to-noise ratio was higher. As the tunnel static pressure was again increased by about a factor of two, to 13.50 kPa, the uncertainty in velocity increased because the signal-to-noise ratio decreased. As the tunnel static pressure was further doubled to 27.56 kPa, the uncertainty in velocity increased even further, with the uncertainty being 45% higher than that observed in the 1.75 kPa case. The decrease in signal-to-noise ratio at the higher pressures is probably caused by the lower concentration of NO and the lower fluorescence yield (ratio of molecules that fluoresce instead of non-radiatively relax to the ground state) as the quenching rate increases at higher pressure. At lower pressures it is possible that the efficiency of the photodissociation process is slow and has not been completed in the 38 ns between the pump and probe pulses, resulting in lower signals.

As static pressure was increased, a proportional increase in average measured velocity was observed. This suggests that a flow was established within the facility as static pressure was increased. If indeed a small flow of gas had been established in the facility in order to increase the pressure, varying the delay time would have allowed us to check this hypothesis.

A quantitative analysis was performed on the average of both the 1st and 2nd exposures single-shot images for each static pressure case shown in Fig. 7 to further explain the trends observed. At the lowest static pressure, the difference between the peak signal at the center of each tagged line and regions between each tagged line (valleys) remained relatively constant at ~40 counts. As the static pressure was increased to 7.06 kPa, the peak-to-valley values increase by a factor of 2 to 3 in both the 1st and 2nd exposure images. At this pressure, the background counts also increased by approximately ~30 counts in both the average of the 1st and 2nd exposures due to stagnant NO gas remaining in the measurement region from shot-to-shot. As the static pressure was increased to 13.50 kPa, the signal and valley levels were both observed to increase, however the difference between the peak and valley counts remained similar to those in the 7.06 kPa case. This effect is attributed to increasing levels of ambient NO gas remaining in the measurement region as the facility static pressure is increased. As the static pressure was further increased to 27.56 kPa, an overall decrease in signal levels was observed accompanied by a decrease in peak-to-valley levels less than that of the lowest static pressure case. Note that signal (and shot noise) from ambient, stagnant NO increased the uncertainty in these static-gas experiments but such signal is not present during the wind tunnel tests in which the NO is continuously being convected downstream. So these uncertainty limits determined in static gas are perhaps larger than would occur in the wind tunnel runs.

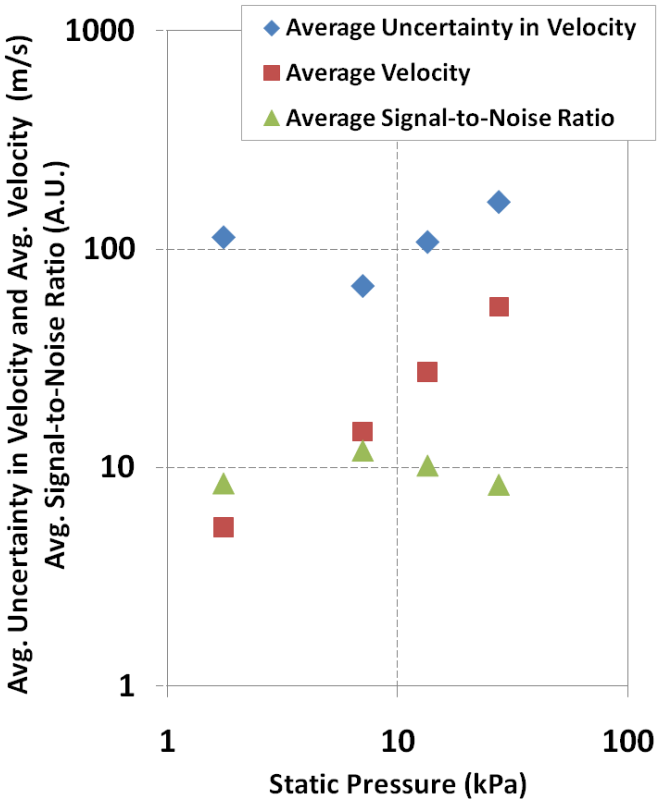

Fig. 7. Average single-shot uncertainty in velocity, velocity, and signal-to-noise ratio as a function of static pressure. Data is averaged from highest ~10% of signal-to-noise ratio values at each pressure condition. Probe beam delay is a constant 1 µs.

IV. Velocity Results

A. Laminar Boundary Layer Measurements

To demonstrate that the $NO_2 \rightarrow NO$ photo-dissociation molecular tagging velocimetry technique is able to accurately measure velocity in a hypersonic boundary layer, a measurement was first performed in an unperturbed laminar hypersonic boundary layer. The laminar nature of the flow using the current wind tunnel model configuration was qualitatively verified with a flow visualization measurement presented in Ref. [21]. Figure 8a shows an experimental flow visualization image from Ref. [21] superimposed with a virtual rendering of the wind-tunnel model. The dotted line shows the relative spanwise position of the measurement plane used in the current experiment. The velocity measurements are made in the wall-normal direction, viewed from the side, along the surface of the plate. Figures 8b and 8c show the average MTV images obtained in both the 1st and 2nd exposures, respectively. The spatial dimensions of the images are: the vertical direction is normal to the model surface; the horizontal image direction is the streamwise flow direction with flow from left to right. The spatial resolution of the measurement was estimated to be 0.14-mm in the vertical direction, which accounts for blurring of signal counts across adjacent rows of pixels on the CCD. The horizontal resolution was estimated to be 0.82-mm and takes into account the displacement and width of the tagged profiles. The angle-of-incidence that the pump laser lines made with the model surface was 15°. The individual excited lines are separated spatially by ~2.3 mm.

Figure 9 shows the mean measured velocity profiles at 4 locations (99.6-mm, 104.2-mm, 113.5-mm, and 115.8-mm, respectively) downstream of the leading edge. The center of each black cross mark indicates the mean measured streamwise velocity (in m/s) parallel to the wall and the wall-normal position (in mm). Due to persistent issues with reflection and scatter at the surface of the plate, the closest measurement location with respect to the

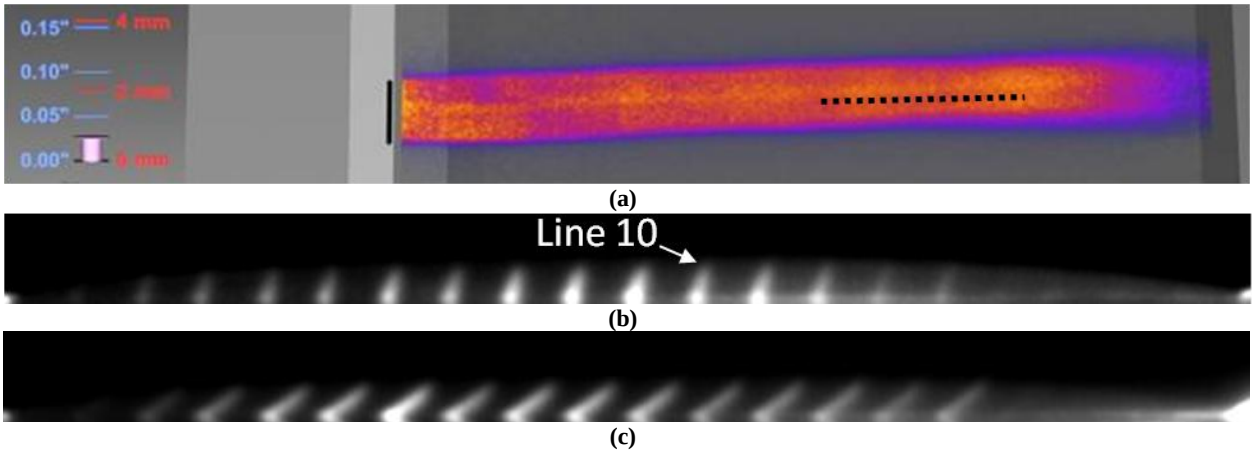

Fig. 8. Flow visualization and raw velocimetry data for laminar boundary layer flow on a flat plate with no trip. The flow visualization image (a) was taken at a plane parallel to and offset 0.7-mm from the model surface. Experimental $NO_2 \rightarrow NO$ photo-dissociation MTV images obtained during the 1st (b) and 2nd (c) exposures in a plane normal to the surface and approximately located in the spanwise position at the black dashed line shown in (a). In all images, flow is from left to right. In (b) and (c) the surface of the plate is near the bottom of the image.

model surface achieved was approximately 0.1-mm. The horizontal width of the black bars centered about each cross mark corresponds to the uncertainty in the mean measured velocity.

For comparison, 3 analytic hypersonic boundary layer profiles (corresponding to the minimum, mean, and maximum wall temperatures measured over the course of the image acquisition sequence) were computed for each of the streamwise measurement locations. Three computations of the analytic profile were made because the temperature measured during image acquisition process increased linearly from approximately 308 K to 350 K. The increasing plate temperature is thought to have had a minimal effect on the accuracy of the mean measured velocity profiles at each location based upon the comparison with the analytic solutions computed for each temperature condition.

As seen in Fig. 9, good agreement with the analytic solutions is observed up to approximately 0.8-mm off of the plate surface. Above 0.8-mm, lines 5, 9, and 10 deviate from the analytic trends, giving a lower measured velocity near the edge of the boundary layer. Since no additional measurement of the boundary layer velocity was made using another measurement technique, it is difficult to determine the cause of the disagreement between the analytic boundary layer solution and the measured mean velocity results. Several potential explanations exist which could describe this behavior. This includes: (1) the edge velocity specified for the analytic solution based on oblique shock relations being dissimilar from the true edge velocity resulting in higher predicted velocities near the boundary layer edge; (2) low signal-to-noise levels (and hence decreased data yield) near the edge of the boundary layer artificially reducing the mean measured value (mean velocity is biased towards low velocity because measurements only occur at the edge when the boundary layer is thicker, and slower, than average); (3) reflected light redirected from the quartz window insert artificially affecting the measurement; (4) the selected blowing rate of NO_2 from the seeding slot affecting the boundary layer thickness and measured velocity near the edge of the boundary layer; (5) bluntness of the leading edge contributing to a discrepancy between the analytic and measured boundary layer profiles; or (6) some combination of all of these factors. In this experiment, the blowing rate of 760 sccm was higher than those typically used for measurements in previous experiments [14,21,27], and is thought to have primarily contributed to the discrepancy between the measured and analytic boundary layer profiles shown in Fig. 9. In Ref. [27], a study of boundary layer thickness versus flow rate of NO was conducted at the same conditions used in Runs 33 and 35. From that study, it was determined that for a blowing rate of 1000 sccm of NO, the boundary layer thicknesses, based on PLIF flow visualizations increased by nearly 18% compared to all measurements made with blowing rates $\leq$ 300 sccm. The Reynolds number based on the edge radius (bluntness) was estimated to be on the order of 20 and is thought to have had a negligible effect on boundary layer thickness. This assumption is based in part on calculations performed in Ref. [28].

Figure 10 shows four single-shot velocity profiles measured 115.8-mm downstream of the leading edge (Line 10). As with Fig. 9, the black cross marks correspond to the measured single-shot streamwise velocities (in m/s) and the wall-normal position (in mm), with the width of the black bars corresponding to the estimated single-shot uncertainty which included an estimate of spatial uncertainty using the linear fit of data provided in Fig. 4. The fit of

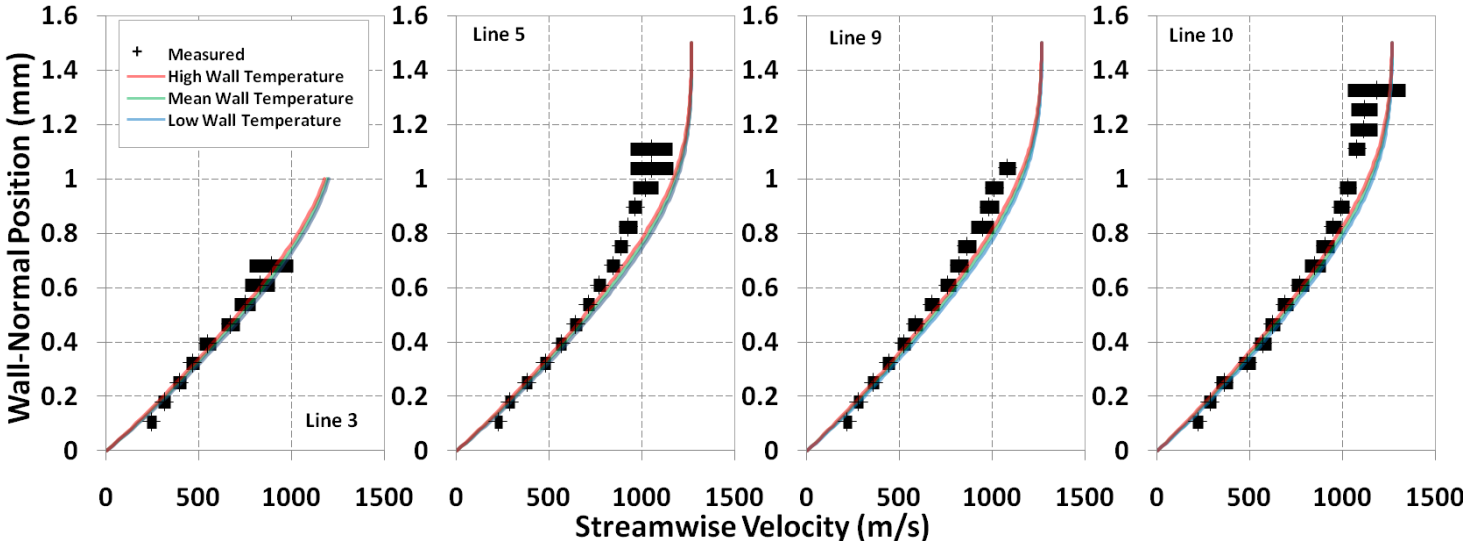

Fig. 9. Mean measured boundary layer velocity profiles (black data points) with no trip mounted on the flat plate. Measurements are shown from lines 3, 5, 9, and 10, located at 99.6-mm, 104.2-mm, 113.5-mm, and 115.8-mm downstream of the leading edge, respectively. The black crosses correspond to the mean velocity and the width of the black bars corresponds to the uncertainty in the mean velocity. The solid red, green, and blue solid lines correspond to the analytic boundary layer solutions using the high, mean, and low temperature wall boundary conditions, respectively.

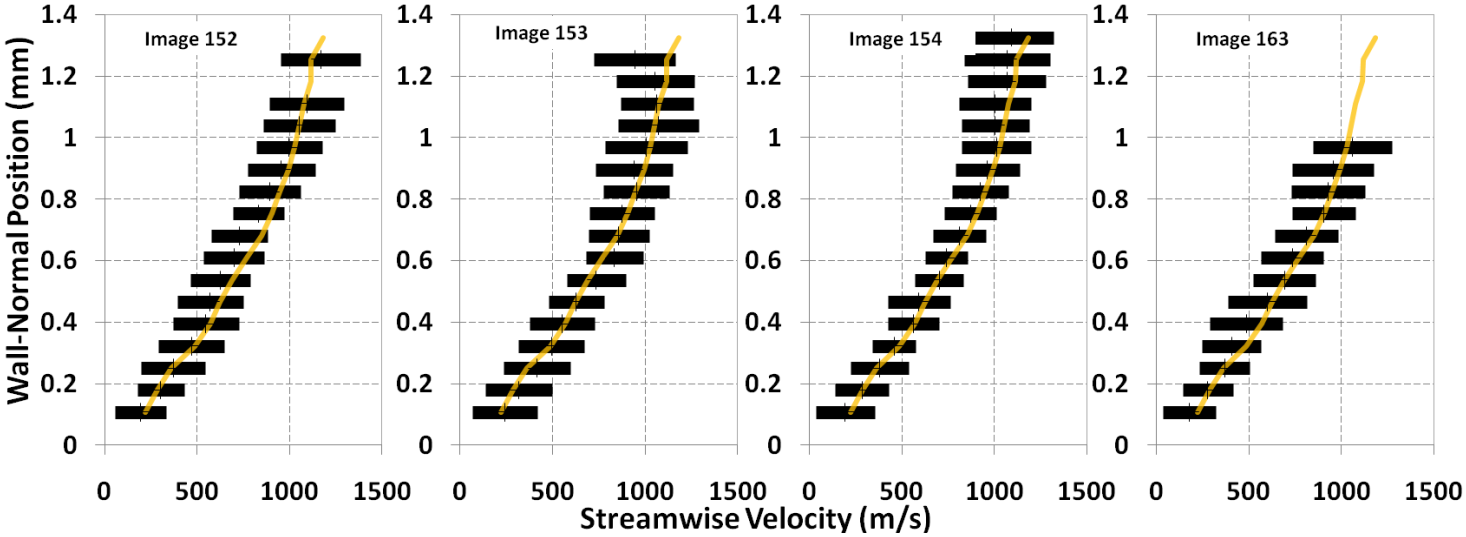

Fig. 10. Single-shot measured boundary velocity profiles with no trip mounted on the flat plate. All measurements were made along line 10, located 115.8-mm downstream of the leading edge. The solid orange line corresponds to the measured mean velocity profile at the same location, also shown in the right panel of Fig. 9.

the experimental data provided in Fig. 4 was used to replace Equation 2 in the calculation of spatial uncertainty for the single-shot velocities. The solid orange line in each plot corresponds to the measured mean velocity profile as shown in Fig. 9. For each of the single-shot profiles plotted in Fig. 10, the single-shot data appears to be centered about the measured mean profile. The absence of data in the plot corresponding to single-shot image 163 near the edge of the boundary layer was due to rejection of low-quality data.

In Fig. 10, the single-shot uncertainty in velocity is relatively large compared to the uncertainty in the mean velocity, shown in Fig. 9. Considering the data in Fig. 10 from image 152 of Run 33 (left-most panel), the average of the uncertainty measured at each point was 170 m/s. An analysis of constituent single-shot uncertainty terms shows that nearly 92.7% of this uncertainty is attributed to the spatial uncertainty in velocity estimated from the data presented in Fig. 4. The remaining single-shot uncertainty consisted of the accuracy (estimated from Fig. 6), magnification, and timing, which represented 6.0%, 1.3%, and 0.6% of the single-shot uncertainty, respectively.

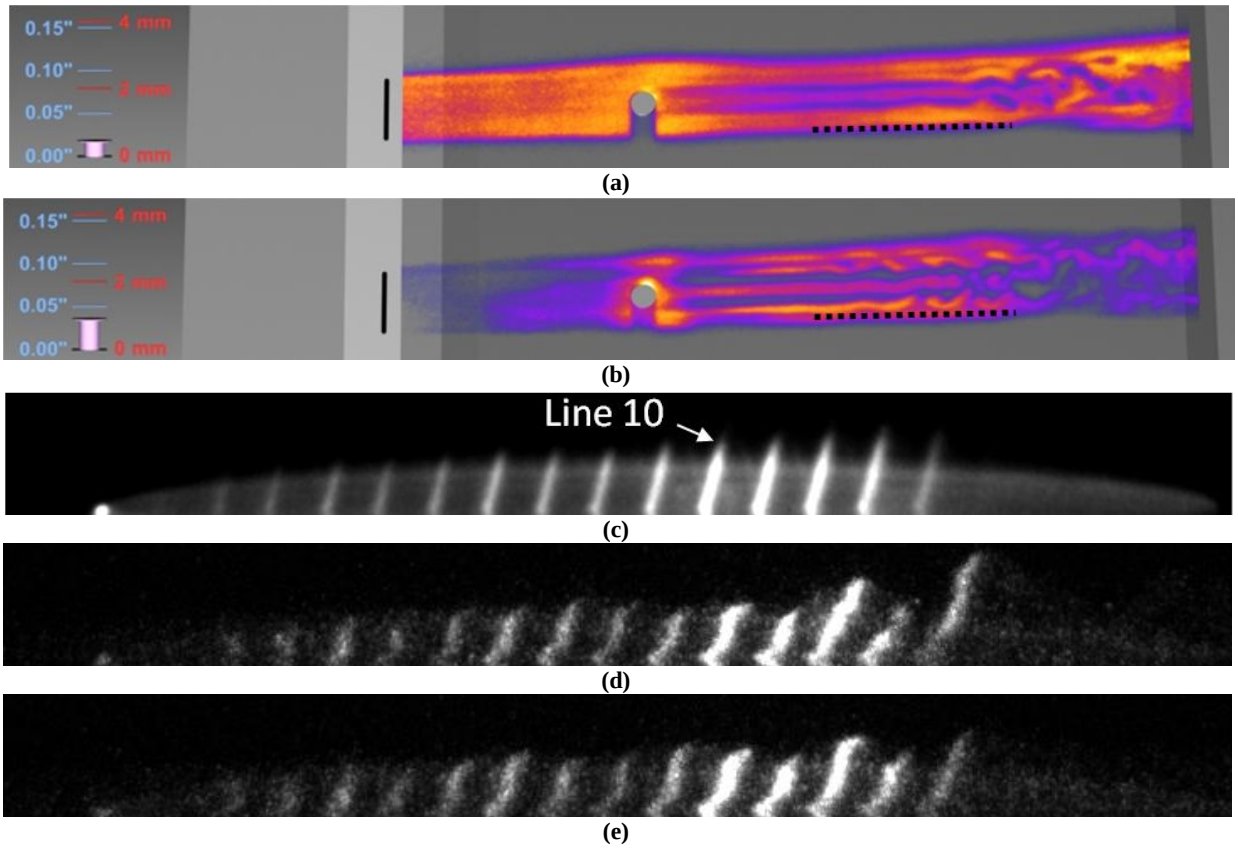

Fig. 11. Flow visualization and raw velocimetry data for boundary layer flow over a 1 mm tall x 4 mm diameter cylindrical trip. Flow visualization images were taken at a plane parallel to and offset (a) 0.5-mm and (b) 1.0-mm from the model surface. Averaged (c) experimental $NO_2 \rightarrow NO$ photo-dissociation MTV images obtained during the 1st exposure and single-shot (d and e) images 33 and 34 obtained during the 2nd exposure in a plane normal to the surface approximately located 6-mm from the model centerline along the dashed line shown in (a) and (b).

B. Laminar-to-Turbulent Boundary Layer Transition Measurements

Figure 11a and 11b shows experimental flow visualization images at measurement planes located 0.75-mm and 1.25-mm off of the model surface, respectively, taken from Ref. [21]. The dotted line in each figure represents the approximate spanwise position of the measurement plane, which was located 6-mm (1.5 trip diameters) from the centerline of the model. Figure 11c shows an average of the single-shot 1st exposure images taken at this measurement plane. Figures 11d and 11e show separate 2nd exposure single-shot images.

Figure 12 shows the mean velocity profile (top-left), several single-shot velocity profiles, and a comparison between the mean velocity profile and each of the single-shot profiles (bottom-right) for one location (Line 10 in Fig. 11c) 113.4-mm downstream of the leading edge. In the plot of mean velocity profile, the baseline analytic laminar boundary layer profile without the trip (solid green line) has been plotted at the same streamwise location for comparison using a measured mean wall temperature of 387 K. This temperature corresponded to the period during the run in which the images were acquired. In the plots of single-shot velocity, the solid orange line corresponds to the mean velocity profile.

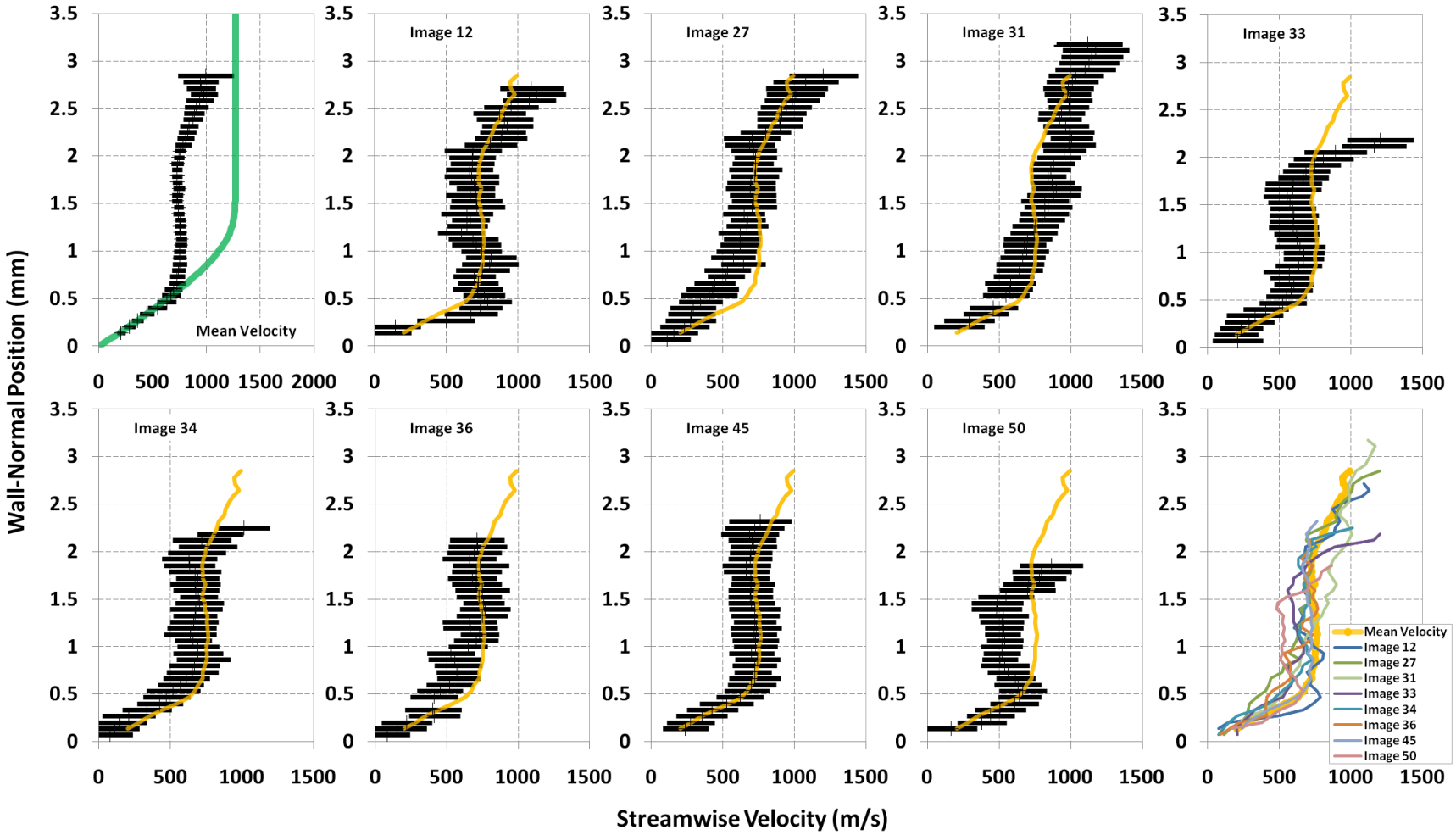

Fig. 12. Mean experimental boundary layer velocity profile (black data points, top-left figure) for line 10, Run 35, with a 1 mm tall x 4 mm diameter cylindrical trip attached to the flat plate. The mean profile is plotted against the baseline analytic laminar solution without the trip (green solid line) in the top left panel. Single-shot experimental profiles (black data points, remaining figures) are plotted against mean experimental profile (orange solid line). The bottom right panel displays all the velocity profiles (without uncertainties) on the same graph.

In the plot of mean velocity (top-left, Fig. 12), the measured profile has the same general trend as the computed analytic and measured laminar profiles up to 0.5-mm above the model surface. Above this point, the mean velocity remains relatively constant, between approximately 670 m/s and 750 m/s, until approximately 2-mm above the plate surface. At this point, the mean velocity profile gradually increases with wall-normal distance. Also above this point, the measured uncertainty in the mean velocity increases with wall-normal distance. From analysis of this plot and the experimental images, we see that the mean boundary layer measured in this flow extends approximately 3 times farther off the model surface than does the laminar profile measured in Run 33. In Ref. [21], Figs. A27 through A29 appear to show that the transitional boundary layer at this spanwise plane location extends 1.75-mm off of the model surface. In this experiment, however, seeded flow structures were observed to intermittently extend beyond 3-mm.

In the single-shot velocity profile plots shown in Fig. 12, each profile approximately follows the mean measured velocity profile very near the wall surface (less than 0.25-mm). As wall-normal distance increases above 0.25-mm, several of the profiles noticeably deviate from the mean measured profile, such as in single-shot images 12, 27, 31, 36, and 50. For all of the single-shot velocity profiles measured, the shift of the center of each of the single-shot profiles with respect to the mean profile was much greater than the single-shot profiles presented from the laminar boundary layer measurement shown in Fig. 10. The bottom-right plot in Fig. 12 shows each of the single-shot profiles plotted against the mean profile. As can be seen from this plot, there is a relatively large level of variability above the 0.25-mm wall-normal position. In additional to measured streamwise variations in velocity, variations in the wall-normal length of the tagged profiles occurred. This indicates that the local concentration of NO produced from photo-dissociation of NO_2 varied both spatially and temporally, possibly resulting in bias in mean velocities at the edge of the boundary layer. Figure 11d and 11e show single-shot images which demonstrate this tagged profile height variation. The variation occurs most noticeably along the last two tagged lines. In Fig. 11d, the fluorescence intensity along the line located 2nd from the right appears to have several lobes of increased signal intensity occurring in the wall-normal direction, indicating a non-uniform distribution of NO, which is not observed in Fig. 11e. Along the right-most line in Fig. 11d, the tagged profile extends much further off the model surface than does the tagged line shown in Fig. 11e at the same streamwise location.

To better understand the sensitivity of the measurement technique for detecting the unsteadiness inherent to the transitioning flow within the boundary layer, a comparison of the standard deviation of measured velocity is provided in Fig. 13. In this plot, only values computed using points totaling more than 25% of the maximum number of data point yield along Line 10 are shown. For the laminar case, the lowest fluctuations are observed at about 1 mm above the model surface where the measured standard deviation is about 5% of the mean velocity at that location. As can be seen in Fig. 13, over the extent to which the laminar profile is measured, the transitioning boundary layer has a level of variability (standard deviation) in streamwise velocity that is consistently 2-3 times higher than the corresponding point in the laminar profile. The maximum velocity variability observed in the transitioning boundary layer flow when comparing the region covered by the extent of the laminar boundary layer occurs approximately at the middle of the laminar profile (0.5 mm). The velocity fluctuations approach 30% of the mean velocity at that location, whereas at the same location for the no-trip case the fluctuations are about 10% of the mean. Above this point, the transitioning boundary layer velocity variability decreases to a constant level which is about 15% of the mean. Above approximately 2-mm, the velocity fluctuations increases by about 50% to about 19% of the mean.

For the laminar boundary layer measurement, the measured fluctuations are, at minimum, 5% of the mean flow measured at the same wall-normal location. This level of fluctuation in the laminar boundary layer, which was expected to be on the order of 1-2%, is higher than anticipated. In addition to signal-to-noise effects, freestream

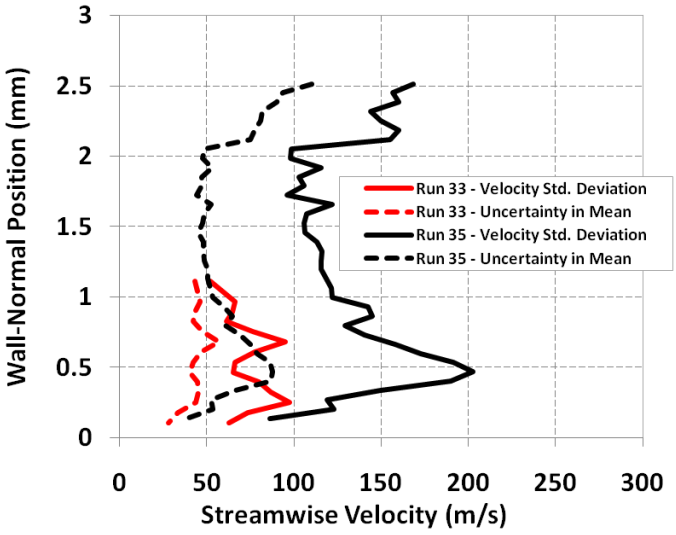

Fig. 13. Comparison of measured velocity standard deviation (solid lines) and total velocity uncertainty in the mean (dashed lines) for laminar (Run 33) and transitioning (Run 35) boundary layer flows.

turbulence, unsteadiness in the NO_2 gas seeding, or unsteadiness induced by jet-crossflow interactions may contribute to this fluctuation. While the most likely cause of these larger-than-expected fluctuations is signal-to-noise effects, the exact cause is unclear and further testing is needed to pinpoint the root cause.

For the transitional boundary layer, a comparison with a numerical simulation, performed in Case II of Ref. [29], and the measurement obtained in Run 35 shows similarities between both the measured mean velocity and the locations of fluctuations within the velocity boundary layer. Figure 14a and 14b show both the streamwise velocity and streamwise root-mean-square (RMS) velocity contour maps obtained from Ref. [29], respectively. These spanwise measurement planes were located 40 mm downstream of the roughness element. The maps are symmetric about the centerline of the model, with only the right half of the computation shown. The flow direction is into the page. For comparison, the spanwise measurement location obtained in Run 35 is denoted by the vertical dashed line in both figures, which was located 38 mm downstream of the roughness element in the experiment. The computation of Ref. [29] was done at the same freestream and post-shock conditions as Run 35, with the only differences between the computation (Case II) and the current measurement being the trip height (2-mm versus 1-mm) and estimate of k/δ (1.3 versus 1.05, respectively).

Analysis of the streamwise velocity contour map in Fig. 14a shows a mushroom-like low-streamwise-velocity structure located between the spanwise positions of z = 4 mm to 7 mm and extending up to y = 3 mm in the wall-normal direction. Along the line corresponding to the approximate measurement location in Run 35, it can be seen that near the wall-normal position of y = 0.5 mm, a large spanwise gradient in streamwise velocity is seen. This location corresponds to the position at which increased fluctuations in streamwise velocity were measured (Fig. 13) and appears to agree qualitatively with the computation shown in Fig. 14b, where a locally high streamwise RMS velocity field is predicted. Along this vertical line between 0.5 mm and 2.0 mm, the computation shows that streamwise velocity is relatively constant (Fig. 14a), in agreement with the experiment. In this same region, a decrease in streamwise RMS velocity (Fig. 14b) is also observed, which also appears to be in agreement with the observation shown in Fig. 13. Above the wall-normal position of y = 2 mm, an increase in wall-normal velocity is observed which agrees with the mean velocity trend presented in Fig. 12. At this same location, an increase is streamwise RMS velocity is predicted (Fig. 14b), which again appears to agree qualitatively with the results of Fig. 13 for the transitional boundary layer measurement. According to the authors in Ref. [29], this streamwise velocity structure is attributed to a horseshoe vortex rolling up on the trip. The vertical dashed line in Fig. 14b corresponds to a cut nearly through the centerline of the vortex. As expected, high levels of streamwise RMS velocity occur near the vortex shear layer, while low RMS streamwise velocity levels are observed near the vortex core. Unfortunately, direct comparisons cannot be made since it is likely that the differences in trip height, and therefore the k/δ values, result in substantial differences in the overall flowfield. Nonetheless, the computations offer some indications that plausibly explain the observed measurements. Further computations are required at the experimental conditions to more confidently explain the measurements. Similarly a more detailed set of measurements would be required to validate the computations.

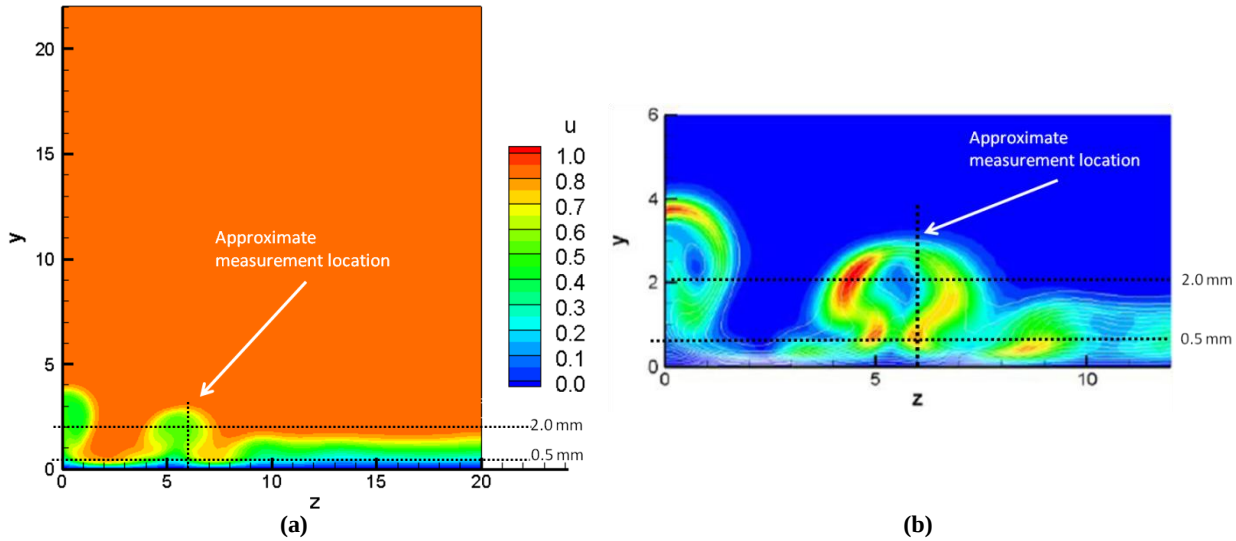

(a) **(b)**

Fig. 14. Spanwise contour maps of streamwise (a) mean and (b) RMS velocity obtained from Ref. [29] located 40 mm downstream of 2-mm tall, 4-mm diameter cylindrical roughness element. The vertical dashed lines correspond to the approximate measurement location in Run 35.

The uncertainty in the mean profiles, also shown in Fig 13 as dashed lines, indicate that the mean profiles are measured with an uncertainty of better than 50 m/s for the laminar case and for much of the outer profile in the transitional case. For the region of largest fluctuation in the transitional case the, the uncertainty is about 80 m/s and exceeds 100 m/s at the far edge of the boundary layer, where the number of measurements included in the average decreases to 25% of the acquired images. At the edge of the boundary layer, bias errors, which are not included in the analysis, could cause inaccurate mean velocities.

V. Discussion

In this experiment, a measurement of both mean and single-shot velocities has been made in laminar and transitional hypersonic boundary layer flows. While the data presented provides insight into the behavior of such flows, several difficulties were encountered during testing which will be outlined in this section in addition to suggested improvements to the experimental setup.

One of the major issues in the experiment was the alignment of 355-nm lines with each of the 226-nm laser sheets. This alignment issue was caused by facility vibrations affecting the alignment optics affixed to the top of the tunnel test section and affected the signal-to-noise levels of the measured profiles. In future experiments, remote controlled, motorized mirror adjustments will be used to improve the accuracy and repeatability of the alignment. The intensity of the laser light at the tunnel test section was also diminished by the use of 6-8 turning prisms which absorbed and reflected 10-30% of the laser energy per prism. Turning mirrors with >99% reflectivity will be used in future experiments to avoid laser energy loss.

Another issue encountered with the measurement was that the 355-nm light and, to a lesser-extent, the 226-nm light, reflected from within the hollow model through the UV window mounted to the model surface. Care was taken to create as long a delay path as possible for the 1st probe beam so that the 1st exposure would capture as little reflected light from the initial pump beam as possible. However, an intermittent 15 ns timing jitter associated with the camera electronics resulted in many of the single-shot images having large signal levels in the viewing region corresponding to the position of the window insert. This in turn affected the signal-to-noise levels measured along each profile. A decision was made prior to processing the images to remove images where reflection was thought to adversely affect the measurement. This resulted in fewer images being available for processing velocity data. To avoid this reflection problem in future experiments, another window will be placed on the lower surface of the model to allow the laser light to pass completely through the model with minimal reflection. This modification might also allow for measurement of velocity closer to the surface.

In this experiment, the ground vibrational state electronic transition of NO was probed as a matter of convenience. In the current experiment, the dye laser used a mixture of Rhodamine 640, which allowed for spectral access of several ground vibrational electronic transitions that are attractive for NO flow visualization, NO MTV, and NO thermometry measurements in addition to the $NO_2 \rightarrow NO$ MTV measurement. This method of spectral operation was preferred because of the relatively short test schedule and the number of objectives which had to be met during the test. However, this approach resulted in excitation of NO in the ground vibrational state present between the tagged lines, which were especially prevalent during static gas testing. This in turn adversely affected the measured signal-to-noise levels, and hence decreased measurement precision during static gas testing. To avoid this, an attractive alternative is exciting the 1st vibration state of NO, as presented in Ref. [18]. This state is relatively well populated for a period after photo-dissociating NO_2. Application of this method requires a change in the dye mixture, such as Rhodamine 610 which is different from that used in the present experiment, in order to probe the appropriate transitions at lower wavelengths.

Based upon the results of Fig. 7, it appears that there is an optimal range of static pressures over which the $NO_2 \rightarrow NO$ photo-dissociation works best, primarily near ~7 kPa. During testing with the wind tunnel operating, poor signal quality was observed at static pressures below approximately 2.76 kPa. While the results presented in Fig. 7 provide some indication of the relationship between signal-to-noise levels and static pressure, the background NO affected the measured signal-to-noise ratio, and thus cannot be used to precisely predict the precision with which velocity can be measured in an actual flow where background NO is not present. The use of the technique in Ref. [18] might allow a more direct reference for characterizing the measurement precision in static gas tests, since it avoids excitation of the ambient, re-circulating NO. In addition to contamination of signal from background NO at higher static pressures, quenching by both NO_2 and NO may contribute to low fluorescence yield. At lower static pressures, the number density of NO_2 available for photo-dissociation may be too low to provide sufficient levels of NO needed for higher signal-to-noise levels. Alternatively, the ground vibration electronic transition of NO used in this study may be insufficiently populated, resulting in lower signal levels. Further testing must be performed to gain a better understanding of the relationship between static pressure, signal-to-noise levels, and velocity precision.

Another potential issue with the analysis presented in this work is the methodology used to compute the signal-to-noise ratio. The use of single peak and valley values of signal to compute the signal magnitude could potentially be affected by non-uniformities in the laser sheet intensity profile (i.e. valley on either side of a profile being unequal). Additionally, the method used to compute the noise level can be affected by non-uniformities in the signal intensity in both the horizontal and vertical directions, such as near the edge of the boundary layer, resulting in higher than expected noise levels. To avoid such potential errors, a better methodology for computing the signal-to-noise ratio, such as a Gaussian fit similar to that presented in Ref. [30], can be used. Another potential solution is to increase the distance between each tagged profile such that the signal intensity in the valleys between the profiles is on the order of the background counts of the camera if no background NO is present.

In this analysis, it was assumed that the flow did not accelerate or decelerate between the 1st and 2nd exposures, allowing for calculation of velocity using Equation 1. However, if the flow is either accelerating or decelerating, the use of Equation 1 to determine velocity is not valid. A potential solution to this would be reporting displacement magnitudes rather than velocities, which could then be compared with gas displacement magnitudes obtained from CFD calculations.

Considering the results of Figs. 4 and 6, it first appears that the most direct solution for reducing spatial uncertainty to less than 10 m/s is to increase the probe beam delay, Δt_{PROBE}, to 50 μs or more. Since the edge velocities approach 1000 m/s or more, however, the profiles can travel 50-mm, resulting in unacceptably large spatial resolution. Therefore, a compromise must be made between the magnitude of spatial uncertainty and spatial resolution acceptable for any experiment. Figure 4 suggests that another way to improve the precision of the technique is to improve the signal-to-noise ratio, which can be accomplished by increasing the signal through improved alignment and higher laser-beam energies and by reducing the noise by rejecting spurious scatter from the 355 nm light (such as by adding an exit window for the model). Another factor that could improve the measurements is the spatial resolution of the measurement. If a higher magnification optical system was used (or if the camera could be moved closer to the centerline) then higher accuracy measurements may result. In the current experiment, a 1 pixel displacement corresponds to a velocity of approximately 75 m/s. Based upon the static gas measurement results, the signal-to-noise levels and reduced magnification made it difficult to obtain sub-pixel velocity accuracies, resulting in spatial uncertainties on the order of 10 m/s. Furthermore, experiments could be operated closer to the optimum static pressure of ~7 kPa. The current experiments were operated with static pressure of about 2 kPa in the boundary layer.

VI. Conclusions

$NO_2 \rightarrow NO$ photo-dissociation molecular tagging velocimetry has been used to make measurements in both a hypersonic laminar and transitional boundary layer. To the author's knowledge, this paper represents the first acquisition of single-shot velocity profiles in a transitional hypersonic boundary layer. Using this measurement technique, measured velocity fluctuations were generally 2-4 times larger in the transitional boundary layer than those measured in a laminar boundary layer with the same edge conditions. The maximum fluctuations occurred at a location corresponding to approximately 50% of the height of the laminar boundary layer. The magnitudes of the fluctuations were approximately 30% of the measured mean velocity. An effort was made to characterize the single-shot precision of the measurement technique at varying probe beam delay settings and static pressure conditions. While the current data set is promising, additional measurements are required to confirm the behavior of hypersonic boundary layer transition measured and better characterize the growth of instabilities leading to such transition as a function of downstream distance. Finally, a more in-depth study of the photo-dissociation process is needed to optimize the precision with which measurements in such flows can be made.

References

[1] Wheaton, B.M. and Schnieder, S.P., "*Roughness-Induced Instability in a Laminar Boundary Layer at Mach 6*," AIAA 2010-1574, 48th AIAA Aerospace Sciences Meeting, Orlando, FL, January 4-7, 2010.

[2] Kegerise, M.A., Owens, L.R., and King, R.A., "*High-Speed Boundary-Layer Transition Induced by an Isolated Roughness Element*," AIAA 2010-4999, 40th Fluid Dynamics Conference and Exhibit, Chicago, IL, June 28 – July 1, 2010.

[3] Hiller, B., Booman, R.A., Hassa, C., and Hanson, R.K., "*Velocity visualization in gas flows using laser-induced phosphorescence of biacetyl*," Rev. Sci. Instrum., 55 (12), pp. 1964-1967, December, 1984. doi: 10.1063/1.1137687

[4] Stier, B., Koochesfahani, M.M., "*Molecular Tagging Velocimetry (MTV) measurements in gas phase flows*," Experiments in Fluids, 26, pp. 297-304, 1999. doi:10.1007/S00348-005-0292

[5] Danehy, P.M., O'Byrne, S., Houwing, A.F.P, Fox, J.S., and Smith, D.R., "*Flow-Tagging Velocimetry for Hypersonic Flows Using Fluorescence of Nitric Oxide*," AIAA Journal, 41 (2), pp. 263-271, February, 2003. doi: 10.2514/2.1939

[6] Dam, N.J., Klein-Douwel, R.J.H., Sijtsema, N.M., and ter Meulen, J.J., "*Nitric oxide flow tagging in unseeded air*," Optics Letters, 26 (1), pp. 36-38, January 1, 2001. doi: 10.1364/OL.26.000036

[7] Boedeker, L.R., "*Velocity measurement by H2O photolysis and laser-induced fluorescence of OH*," Optics Letters, 14 (10), pp. 473-475, May 15, 1989. doi: 10.1364/OL.14.000473

[8] Pitz, R.W., Brown, T.M., Nandula, S.P., Skaggs, P.A., DeBarber, P.A, Brown, M.S., and Segall, J., "*Unseeded velocity measurement by ozone tagging velocimetry*," Optics Letters, 21 (10), pp. 755-757, 1996. doi: 10.1364/OL.21.000755

[9] Miles, R., Cohen, C., Connors, J., Howard, P., Huang, S., Markovitz, E., and Russell, G., "*Velocity measurements by vibrational tagging and fluorescent probing of oxygen*," Optics Letters, 12 (11), pp. 861-863, November, 1987. doi: 10.1364/OL.12.000861

[10] Barker, P., Bishop, A., and Rubinsztein-Dunlop, H., "*Supersonic velocimetry in a shock tube using laser enhanced ionization and planar laser induced fluorescence*," Appl. Phys. B, 64 (3), pp. 369-376, 1997. doi: 10.1007/s003400050186

[11] Littleton, B.N., Bishop, A.I., McIntyre, T.J., Barker, P.F., and Dunlop-Rubinsztein, H., "*Flow tagging velocimetry in a superorbital expansion tube*," Shock Waves, 10, pp. 225-228, 2000.

[12] Koochesfahani, M.M. and Nocera, D.G., "Molecular Tagging Velocimetry," *Handbook of Experimental Fluid Dynamics*, edited by Foss, J., Tropea, C., and Yarin, A., Springer-Verlag, Berlin, 2007, Chap. 5.4.

[13] Bathel, B.F., Danehy, P.M., Inman, J.A., Jones, S.B., Ivey, C.B., and Goyne, C.P., "*Multiple Velocity Profile Measurements in Hypersonic Flows Using Sequentially-Imaged Fluorescence Tagging*," AIAA Paper 2010-1404, 48th AIAA Aerospace Sciences Meeting, Orlando, FL, January 4-7, 2010.

[14] Bathel, B.F., Danehy, P.M., Inman, J.A., Watkins, A.N., Jones, S.B., Lipford, W.E., Goodman, K.Z., Ivey, C.B., and Goyne, C.P., "*Hypersonic Laminar Boundary Layer Velocimetry with Discrete Roughness on a Flat Plate*," AIAA Paper 2010-4998, 40th Fluid Dynamics Conference and Exhibit, Chicago, IL, June 28 - July 1, 2010.

[15] Orlemann, C., Schulz, C., and Wolfrum, J., "*NO-flow tagging by photodissociation of NO2. A new approach for measuring small-scale flow structures*," Chem. Phys. Lett., 307, pp. 15-20, 1999.

[16] Shinji, N., Kasahara, M., Tsue, M., and Kono, M., "*Velocity Measurements of Reactive and Non-reactive Flows by NO-LIF Method Using NO_2 Photodissociation*," Heat Transfer – Asian Research, 34 (1), pp. 40-52, 2005. doi: 10.1002/htj.20038

[17] Hsu, A.G., Srinivasan, R., Bowersox, R.D.W., and North, S.W., "*Two-component molecular tagging velocimetry utilizing NO fluorescence lifetime and NO2 photodissociation techniques in an underexpanded jet flowfield*," Applied Optics, 48 (22), pp. 4414-4423, August, 2009.

[18]Hsu, A.G., Srinivasan, R., Bowersox, R.D.W, and North, S.W., "*Molecular Tagging Using Vibrationally Excited Nitric Oxide in an Underexpanded Jet Flowfield*," AIAA Journal, 47 (11), pp. 2597-2604, November, 2009. doi: 10.2514/1.47716

[19] Jiang, N., Nishihara, M., and Lempert, W.R., "*500 kHz NO_2 Molecular Tagging Velocimetry in a Mach 5 Wind Tunnel*," AIAA 2010-4348, 27th AIAA Aerodynamic Measurement Technology and Ground Testing Conference, Chicago, IL, June 28 – July 1, 2010.

[20] Micol, J.R., "*Langley Aerothermodynamic Facilities Complex: Enhancements and Testing Capabilities*," AIAA 1998-0147, 36th AIAA Aerospace Sciences Meeting, January 12-15, 1998, Reno, Nevada.

[21] Danehy, P.M., Ivey, C.B., Inman, J.A., Bathel, B.F., Jones, S.B., Jiang, N., Webster, M., Lempert, W., Miller, J., and Meyer, T., "*High-speed PLIF imaging of hypersonic transition over discrete cylindrical roughness*," AIAA 2010-0703, 48th AIAA Aerospace Sciences Meeting, Orlando, FL, January 4-7, 2010.

[22] Danehy, P.M., Alderfer, D.W., Inman, J.A., Berger, K.T., Buck, G.M., and Schwartz, R. J., "*Fluorescence Imaging and Streamline Visualization of Hypersonic Flow over Rapid Prototype Wind-Tunnel Models*," Proc. IMechE, Part G: J. Aerospace Engineering, 222(G5), 637-651, 2008.

[23] Sanchez Sorzano, C.O., Thevenaz, P., and Unser, M., "*Elastic Registration of Biological Images Using Vector-Spline Regularization*," IEEE Transactions on Biomedical Engineering, 52 (4), pp. 652-663, April, 2005.

[24] Rasband, W.S., ImageJ, U. S. National Institutes of Health, Bethesda, MD, USA, http://rsb.info.nih.gov/ij, 1997-2009.

[25] Bathel, B.F., Danehy, P.M., Inman, J.A., Jones, S.B., Ivey, C.B., and Goyne, C.P., "*Velocity Profile Measurements in Hypersonic Flows Using Sequentially-Imaged Fluorescence-Based Molecular Tagging Velocimetry*," AIAA Journal (to be published).

[26] Inman, J.A., Bathel, B.F., Johansen, C.T., Danehy, P.M., Jones, S.B., Gragg, J.G., and Splinter, S.C., "*Nitric Oxide PLIF Measurements in the Hypersonic Materials Environmental Test System (HYMETS)*," AIAA 2011-1090, 49th AIAA Aerospace Sciences Meeting, Orlando, FL, January 4-7, 2011.

[27] Danehy, P.M., Bathel, B., Ivey, C., Inman, J.A., and Jones, S.B., "*NO PLIF study of hypersonic transition over a discrete hemispherical roughness element*," AIAA 2009-0394, 47th AIAA Aerospace Sciences Meeting, Orlando, FL, January 4-7, 2009.
[28] Balakumar, P., "*Stability of Supersonic Boundary Layers Over Blunt Wedges*," AIAA 2006-3053, 36th AIAA Fluid Dynamics Conference, San Francisco, CA, June 5-8, 2006.
[29] Chang, C.L., Choudhar, M.M., and Li, F., "*Numerical Computations of Hypersonic Boundary-Layer over Surface Irregularities*," AIAA 2010-1572, 48th AIAA Aerospace Sciences Meeting, Orlando, FL, January 4-7, 2010.
[30] Ramsey, M.C. and Pitz, R.W., "*Template matching for improved accuracy in molecular tagging velocimetry*," Experiments in Fluids, 6, May, 2011.
doi: 10.1007/s00348-011-1098-y